applied sciences

MDPI

Article

A Free-Space Transmission Setup for Material Parameters Estimation with Affordable and Non-Synchronized Software-Defined Radios in the 0.85–1.55 GHz Band

Fábio Júlio Fonseca Gonçalves [1,*], Adriana Brancaccio [2], Leonardo Augusto Ferreira [3] and Elson José da Silva [4]

1 Federal Institute of Education, Science and Technology of Minas Gerais, Ibirité 32407190, Brazil
2 Department of Engineering, University of Campania, 81031 Aversa, Italy
3 Graduate Program in Electrical Engineering, Federal University of Minas Gerais, Belo Horizonte 31270901, Brazil
4 Department of Electrical Engineering, Federal University of Minas Gerais, Belo Horizonte 31270901, Brazil
* Correspondence: fabio.goncalves@ifmg.edu.br

Abstract: This paper describes a prototype of a free-space transmission setup for dielectric parameters estimation. The transmitter and receiver, both configurable by software and working in the range 0.85–1.55 GHz, are not synchronized, as they use different clocks. An estimation of the dielectric permittivity of a planar sample was obtained by comparing our measurements with a numerical model. A parametric study with different variables was conceived in order to find the best fit between measurements and simulations. Customized techniques were applied to deal with noise and inconsistencies found in the measurements. The genetic algorithm was used to adjust the constants that minimized the error between simulated and experimental data. Results for a reference sample of polymethylmethacrylate are presented and discussed. Although the accuracy of the proposed approach in recovering the dielectric parameters of the sample was relatively low, the simplicity and cost-effectiveness of this setup make it interesting for scenarios where a rough characterization of the material is sufficient.

Keywords: free-space method; materials characterization; software-defined radio

check for updates

Citation: Gonçalves, F.J.F.; Brancaccio, A.; Ferreira, L.A.; da Silva, E.J. A Free-Space Transmission Setup for Material Parameters Estimation with Affordable and Non-Synchronized Software-Defined Radios in the 0.85–1.55 GHz Band. *Appl. Sci.* **2023**, *13*, 3010. https://doi.org/10.3390/app13053010

Academic Editor: Christos Bouras

Received: 26 January 2023
Revised: 14 February 2023
Accepted: 22 February 2023
Published: 26 February 2023

1. Introduction

The characterization of materials using a free-space method is based on the reflection and/or transmission of electromagnetic waves by/through a sample of the material placed in the air at some distance from the transmitting/receiving antennas [1]. This technique is contactless, non-destructive, and can be used over a wide frequency range [1–5]. The possibility of performing non-invasive and contactless in situ measurements is useful in many fields of application, including the characterization of building materials in propagation modeling [6], remote sensing of structural health and through-the-wall imaging [7,8] and the characterization of materials at high temperatures [9].

Despite these advantages, there are issues regarding free-space wave propagation that need to be addressed to correctly formulate our problem. First of all, when these measurements are performed in an ordinary non-anechoic environment, care should be taken to avoid results being affected by noise and unwanted reflections [1]. Furthermore, sample size dictates the choice of the propagation model, where geometrical optics applies to cases of high frequency (small wavelength), whereas full wave or numerical models should be adopted in cases where the dimensions are comparable with the wavelength.

Another issue with free-space wave propagation is the hardware, because microwave equipment and fixtures such as vector network analyzers [10], antennas [11], phase-stable cables [2] and precision positioning systems are quite expensive.

Regarding the electronics of the measurement setup, software-defined radios (SDR) are becoming an interesting and flexible alternative for projects in microwave frequencies [12], such as the measurement of antennas [13] and radar systems [14,15], including ground-penetrating radar (GPR) for soil characterization [16] and landmine detection [17]. SDR can also be used for materials characterization, as shown in [18], though not in free space in this case.

Most of the abovementioned references use a single radio platform containing both a transmitter (Tx) and a receiver (Rx). This configuration is favorable because it ensures synchronization between the Tx and Rx, thus providing coherent measurements [19].

In this work, we investigate a setup with two separate Tx and Rx radios in the 0.85–1.55 GHz range, which costs considerably less than the most commonly adopted solutions. In particular, we focus on the comparison between our measurements and simulated data, with the aim of understanding the impact of the different parameters on the measurements, and, ultimately, assessing the possibility of recovering unknown material parameters from data measured in realistic conditions.

Indeed, the frequency was low and its range was narrow compared with the recent literature [5,20,21]. The working frequencies are limited by low-cost devices. However, we intentionally kept the setup as simple as possible, as an alternative to complex, expensive free-space-based measurement setups. For the sake of simplicity and due to the narrow bandwidth, we assumed that the material was not dispersive. It should be noted that the type of device (software-defined radio) used in this work is not commonly used for materials characterization. Indeed, the main contribution of this paper is to provide free-space materials characterization based on software-defined radios. Moreover, a transmission-only configuration was considered. This entailed having less information than in other contexts, such as ones mentioned in previous papers where all four S parameters [5] or two different incident angles [20] are exploited.

In this context, the role of the computational electromagnetics model was crucial [22]. When working with simple devices, a realistic simulation model should include: (a) a phase shift due to incorrect positioning; (b) a frequency-dependent phase shift; (c) unknown complex permittivity of the nearby floor affecting multipath propagation; (d) limited bandwidth; and (e) measurements with limited quality because of the number of bits in the analog–digital converter (ADC).

In summary, the purpose of this work is to introduce a low-cost free-space transmission setup with separate commercial transmission and reception hardware, and to present a comparison between experimental data and a 2D model simulated by the finite element method (FEM) [22]. Explicit contributions include the description of a customized free-space solution, which is based on simple programmable hardware in the 0.85–1.55 GHz range, as well as a discussion of the computational model that provides data for comparison with the experimental data. This comparison provides insight into the roles of the different parameters involved in the measurement and estimation procedures and may be used as a reference for further works.

This paper is organized as follows: Following the introduction, we descibe the methodology, where the theoretical concepts and experimental details are described, both for the simulation and measurement. This is followed by the results and discussion, where a parameter study is presented and measurements and optimization are shown. Finally, we conclude with general comments about our experience with this setup and about the proposed approach.

2. Methodology

2.1. Experimental—Electromagnetics

2.1.1. General Description

The transmission measurement configuration, where the transmitting and receiving antennae are placed one in front of the other at a fixed distance and the material under test (MUT) is placed between the antennas, is considered (see Figure 1). It is worth underlining that the transmission-only configuration is dictated by the unidirectional nature of the radios in use, which exploits the so-called simplex configuration, where one radio only transmits and the other only receives.

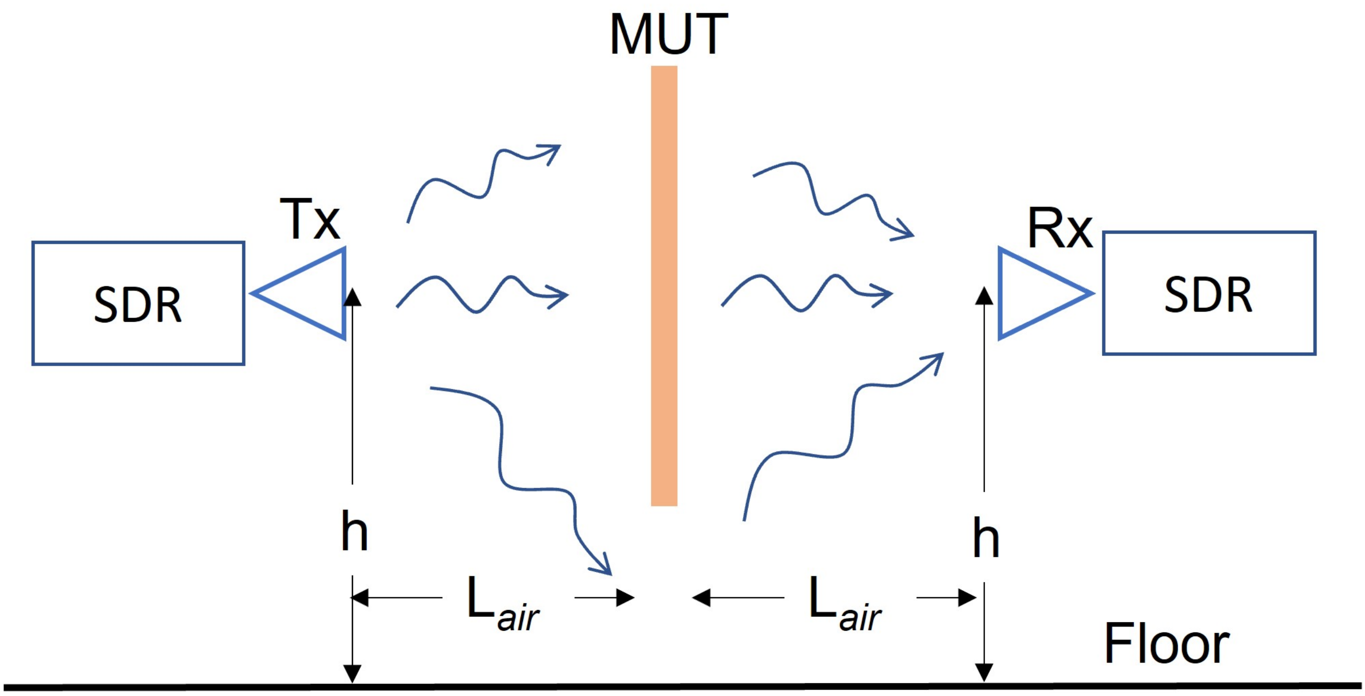

Figure 1. Sketch of the measurement configuration. The MUT is centered between the Tx and Rx antennae, at some distance from the floor.

Measurements of the transmission coefficient S_{21} provide information about MUT dielectric parameters. In order to correctly measure S_{21}, a calibration stage is required. A typical free-space calibration involves the use of measurements made in a reference setup. In the following, we consider the empty setup (denoted as AIR) and the metal plate (MET) [23]. The former mimics the maximum transmission condition (ideally one); the latter represents the minimum transmission condition (ideally zero). The calibration permits the MUT response to be isolated from systematic effects [2,10].

A 305 × 305 × 10.18 mm flat polymethylmethacrylate (PMMA) sample was used as the MUT, with a relative real permittivity of $\varepsilon_r = 2.61$ [8,23,24] and low imaginary part reported to be about 0.01 [8,23] to 0.05 [24]. The sample was obtained from a cut of the same material used in [23], but in that study, its dimensions were 500 × 500 × 10.18 mm. Note that in a free-space setup, the transverse dimensions of the sample play an important role and cannot be significantly reduced [1].

The frequency interval, ranging from 850 MHz to 1.55 GHz, is limited by the antennae (lower bound) and the receiver hardware (upper bound). For simplicity and lowered costs, printed circuit board commercial log-periodic antennae were used, instead of the more common horns similar to the ones used in [23]. A picture of the experimental setup is shown in Figure 2.

Wide samples would greatly simplify the free-space method because the propagation could be modeled by plane waves [1]. However, it is difficult to have a compact setup with these characteristics in the frequency range under study. There, such a premise was dismissed in this work. The distance of each antenna from the surface of the MUT, which was centered between the antennas, was $L_{\mathrm{air}} = 48$ cm, kept consistent as what was used in [23]. The two antennae and the center of the MUT were $h = 45$ cm above the floor (Figure 1).

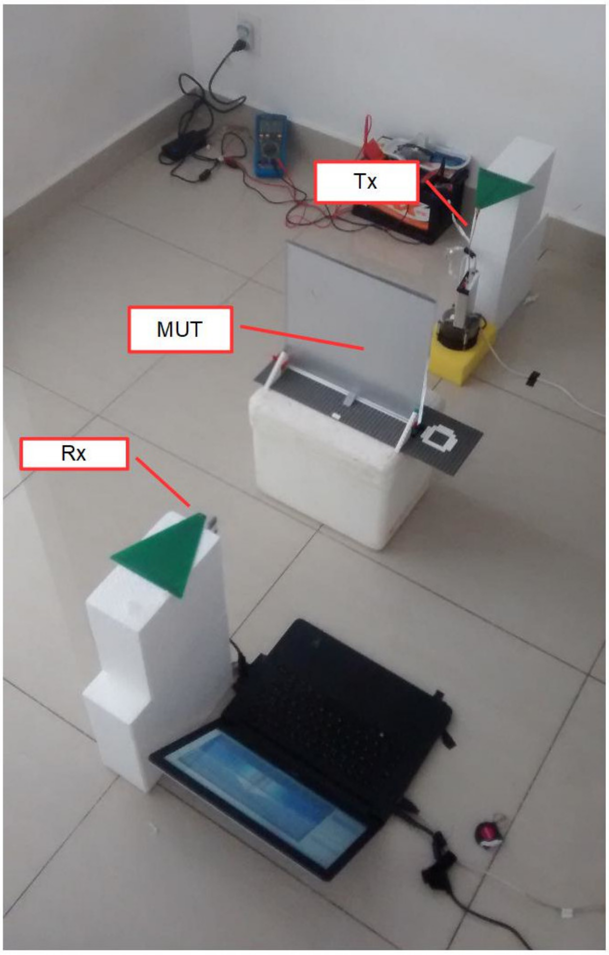

Figure 2. The free-space setup. The antennae and material are held by low permittivity blocks (extruded polystyrene foam) and small plastic pieces. From top to bottom, we have the battery for powering the transmitter (Tx), the Tx itself, the slab of the material in the center of the setup, the receiver (Rx), and the computer that controls the radios and measurements. In the photo, there is metal foil on the surface of the MUT; thus, this is the MET configuration.

2.1.2. Effects on the Signals

Some causes of error on the measurements and the precautions employed to counter their effects on the signal of interest are listed below:

(a) Noises from the power supply: the power supply, which is required to be a 5 V DC, may present ripples, spikes and transients that induce noises on the synthesized signal. For instance, the presence of spurious signals (spurs) [12] may arise due to the power supply ripple modulating the output signal. In order to minimize these overall effects, we used a 12 V battery with integrated circuit regulation to 5 V. This integrated circuit was connected to a heat sink with water cooling to avoid heating. The Rx was connected to a laptop computer, which was powered only by its battery during the measurements. Moreover, ferrite beads were also used in the power and data cables in order to reduce the chance of electromagnetic interference. The experimental setup is shown in Figure 2.

(b) Non-shielded Tx: as the adopted synthesizer was in a low-cost prototyping board with not much protection against incoming or generated electromagnetic interference, an aluminum case was used to better isolate it from the environment (see Figure 3). The Tx circuitry case was placed as far as possible from the Tx antenna to minimize interference. Additionally, as it was elongated, it was positioned perpendicularly to the polarization of the antenna. A 20 cm RG316 coaxial cable was used to connect them, as in Figure 4.

(c) Phase noise and thermal drift: the temperature variation, which is a source of a lot of noise, was reduced by the use of custom heatsinks. For this, an aluminum heatsink placed the transmitter's oscillator crystal in contact with the inside of the case, which is a good thermal conductor and has sufficient mass and area for heat dissipation.

The receiver is already commercially available in a well-finished aluminum case, which is designed for some heat dissipation. However, due to its compactness and the demanding streaming processes of the captures, the radio was still warming up initially. Therefore, we connected its case to two external aluminum heatsinks. They were assembled vertically in order to maximize the contact area for heat transfer and to cause less interference on the radiation patterns of the nearby horizontally polarized antenna—see Figure 5. Wherever applicable, thermal paste was used to increase the heat transfer between the metallic surfaces.

In order to have more compactness and mechanical stability, and to avoid delay and loss in the received signal due to cables, the receiving antenna was directly connected to the Rx SDR, using only an adapter to match the gender of the connectors, as shown in Figure 5.

Figure 3. Detail of the transmitter board inside the aluminum case. The USB connector (universal serial bus), used for receiving configurations from the computer, and two RF SMA connectors [2] (only one was used and the other was turned off during the tests) are shown. The power connector is on the right.

Figure 4. The Tx radio is connected to the transmitting antenna by an SMA RG316 coaxial cable. On the left is the connection to the power supply (battery is partially shown); on the right is the USB cable going to the computer (during the tests, its connector was placed inside the case to improve shielding).

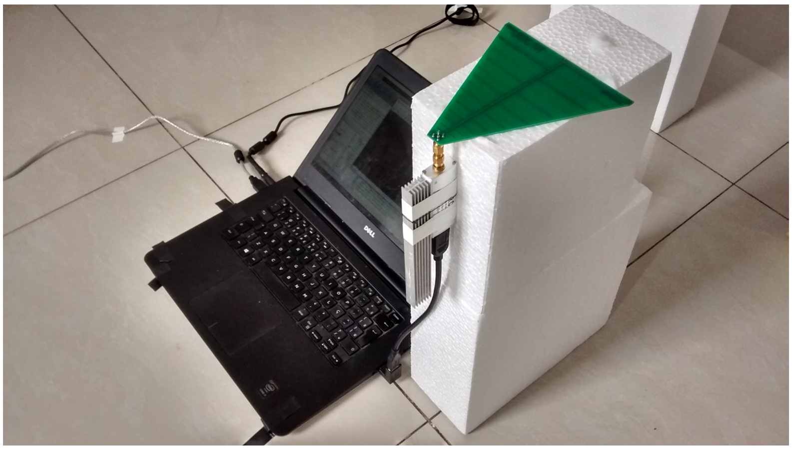

Figure 5. The Rx radio is connected to the receiving antenna and computer via a USB cable. On the left of the computer, we see a second USB cable that is connected to the Tx radio (not shown in photo).

2.2. Experimental—Configurable Hardware

Different user interfaces can be used to perform the configurations and obtain the sampled signals, such as MATLAB [25], GNU Radio [26] or other software. Here, we use MATLAB as it permits us to integrate the whole process, that is, the configuration of Tx, configuration of Rx, signal processing, and data analysis. Finally, a comparison with simulated results was performed using the same software.

The transmitter was an ADF-4351 synthesizer in an evaluation board connected to a computer via USB. A microcontroller CY7C68013A-56PVXC was responsible for communication with the computer and for updating the registers of the ADF-4351, in order to generate the correct frequency tone with the other related attributes specified in the software [27].

The ADF-4351 has an integrated voltage-controlled oscillator (VCO) with a fundamental output frequency ranging from 2.2 to 4.4 GHz. Divide-by-2^n circuits allow the user to generate the RF output frequencies, where $n = 0, 1, 2, 3, 4, 5, 6$ [27].

In order to realize these configurations in the hardware, we used *pyadf435x*, a suite of software and firmware to control the Analog Devices ADF435x series of wide-band RF synthesizers [28]. Additional libraries were installed on the computer and a specific function was written in order to integrate them with MATLAB in a Windows operational system. This permitted the *pyadf435x* routines, which are in the Python language, to be called from MATLAB with all the arguments in the correct data types.

In this way, the main code controlled the frequency sweep and settings of both Tx and Rx, accordingly.

The receiver was an ordinary RTL-SDR [25]. The radios were configured to perform a frequency sweep. The Rx was configured to tune in on the same frequency generated by the Tx, making a frequency correction if necessary. Then, once a frequency value was fixed, the measurement was started and the corresponding samples were saved.

The Rx front-end could work up to a sample rate of 3.2 MHz [25]. However, as this maximum sample rate is more subject to errors, including dropped samples [25], in this work, we used a sample rate of 2.56 MHz. In order to keep integer multipliers, the number of samples per frame (frame length) was defined to be $25,600$. In order to have a redundant database, the frame acquisition was repeated 10 times. Therefore, for each frequency, there are $10 \times 25,600 = 256,000$ complex samples (real and imaginary parts). They were quantized within $2^8 = 256$ levels as the receiver had an 8-bit ADC [12,25]. The real and imaginary parts were available as the I (in phase) and Q (quadrature) components [25].

This process was repeated for the next frequency and so on, for a total number of 71 equally spaced frequencies within the 0.85–1.55 GHz band, resulting in a 10 MHz step. Tx power was set to 2 dBm and Rx tuner gain was set to 0 dB, without automatic gain control (AGC).

About an hour was spent on each configuration, including the intervals for saving data. Some of the captures were corrupted by oscillations that occurred immediately after changes in the frequency, during the sweep or by other unknown errors. Extending the test, however, presented the possibility of the batteries discharging, or other computational problems such as buffers dropping data packets.

Once the data were saved, an analysis could be made based on all of the captures or on part of them, discarding, for instance, the first captures that were are more subject to errors. Using statistics or filtering could also be applied, taking average values amongst samples or fitting the signal to a sinusoidal wave.

2.3. Model and Simulation

In order to simplify the computational model, a two-dimensional (2D) geometry was adopted, where the scene was assumed to be constant along the direction parallel to the floor and to the MUT sheet. The domain of the problem, as shown in Figure 6, was bounded by perfect matched layers (PMLs) [22], simulating an open environment. The antennae and center of the MUT were at $h = 0.45$ m above the floor. However, as this distance was not quite far enough, a multipath propagation should be considered. To this end, we incorporated a 10 cm layer at the bottom of the geometry, in which the complex permittivity of the building material of the floor, i.e., concrete, could be set to approximate the overall effect. A study regarding the adopted values is described in the next section.

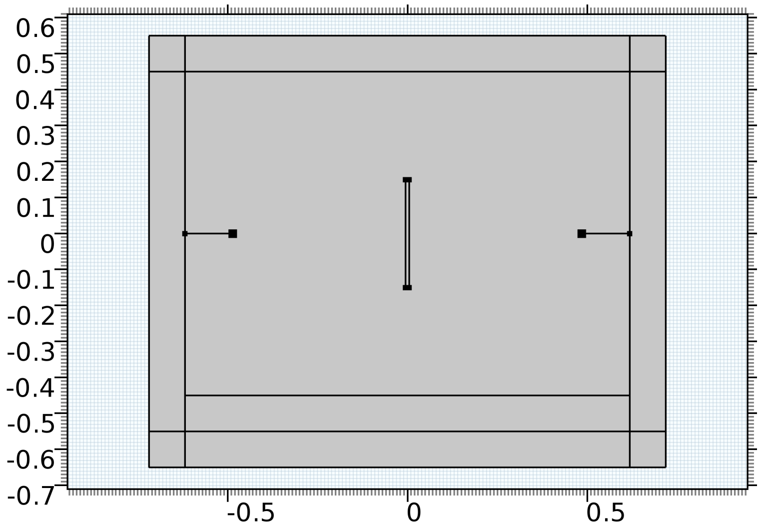

Figure 6. Computational domain of the problem: a rectangular region is bounded by PML (top, bottom, left and right), with the floor just above the bottom PML. The MUT is centered in the middle of the domain; the Tx antenna is on the left and the Rx antenna is on the right. The in−plane coordinates x (horizontal) and y (vertical) are in meters.

The 2D electromagnetic wave equation governs the propagation in the domain [29], as in Equation (1), where μ_r is the relative magnetic permeability, $\mathbf{E}$ is the electric field, k_0 is the free-space wavenumber, ε_r is the relative electric permittivity, ω is the angular frequency, σ is the conductivity of the material and ε_0 is the free-space electric permittivity.

$$\nabla \times \mu_r^{-1}(\nabla \times \mathbf{E}) - k_0^2\left(\varepsilon_r - \frac{j\sigma}{\omega\varepsilon_0}\right)\mathbf{E} = 0. \tag{1}$$

The software COMSOL Multiphysics was used to solve the problem by the finite element method (FEM) [22], with MATLAB routines controlling the variable parameters in order to simulate different scenarios, as discussed later in this section. The solution was provided in terms of a scattered electric field in the frequency domain. The electric field was polarized along the z-axis, being the coordinates x and y in the plane of the model and the coordinate z out-of-plane. In order to simulate the transmitting antenna, an incident

Gaussian beam of unitary amplitude $\mathbf{E}_{bg0} = (0\hat{x}, 0\hat{y}, 1\hat{z})$ V/m, focused along the x-axis, was assumed. The beam radius r is defined by Equation (2), where w_0 is a parameter whose value was varied to test different Gaussian radii on the model.

$$r = \frac{w_0 2\pi}{k_0}. \tag{2}$$

The focus (origin of the beam) was slightly displaced to be just outside of the air domain, in order to avoid the singularity of a punctual source inside the domain.

According to the experimental setup, when the configuration is AIR, i.e., when there is no material sheet placed between the antennae, the MUT region in the simulation is set to be simply air, just as the major part of the domain. On the contrary, when the configuration is MUT, its dielectric properties are used. Finally, when the configuration is MET, the left interface of the MUT region is set as PEC (perfect electric conductor) [22], corresponding to the thin metal foil used in the experiment.

A physics-controlled mesh was used, with a 0.1 wavelength as the maximum element size. Special refinement was performed where the fields were more subject to variation due to the small parts of the geometry or interfaces between materials (see Figure 7), resulting in 76,576 triangular elements. The normalized quality of these elements was 0.6942 (minimum) and 0.974 (average), on a scale where the maximum value of 1 means a perfect equilateral triangle, that is, fewer errors in the FEM.

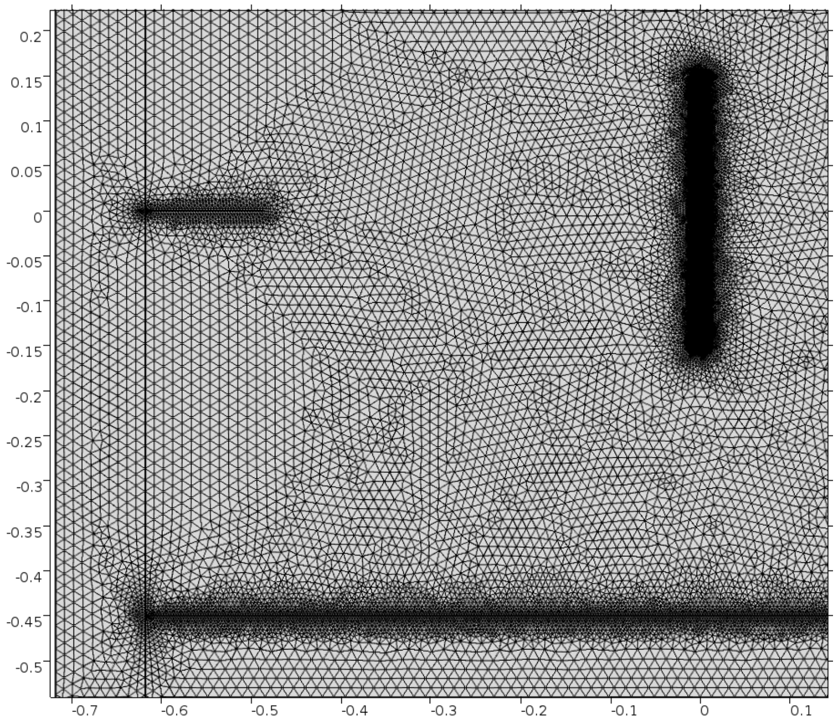

Figure 7. FEM mesh refinements near the regions of the Tx antenna (top left), MUT (top right) and interface air/floor (bottom). The coordinates x (horizontal) and y (vertical) are in meters.

2.4. Parametric Study

A 2D model was simulated for different values of the involved variables, in order to perform a parametric study and gain better understanding of the experimental data set. First of all, the parameter w_0 in Equation (2) was set to be 0.1, 0.2, 0.3 and 0.4. As mentioned before, this controls the radius of the Gaussian beam and, therefore, controls the directivity of the simulated antenna. This approximation avoided modeling the details of the real antenna.

Secondly, as a small misalignment in the focus and/or the sample can introduce significant phase error, we considered 14 different positions of the virtual probe in the simulation, with separations of 1 cm and all of them corresponding to possible positions within the limits of the Rx antenna, which was about 14 cm long.

Finally, as the setup was not far from the floor ($h = 45$ cm), the same floor's unknown complex permittivity was considered as a variable, with the possible values $2, 3, 4, 5, 6$ and 7 for the real part and $0, 0.1, 0.2, 0.3$ and 0.4 for the imaginary part. These ranges are based on reported values for building materials, which is concrete, in this case [30,31]. It must be stressed that our intention here was not to retrieve the properties of the floor. Instead, we investigated whether an estimation would help to model the problem around the MUT.

2.5. Optimization

A comparison between the measured data and the corresponding simulated data allows us to find the optimal values of the parameters to tune the simulations to the measurements. To this end, an optimization routine was used to approximate the constants, making the experimental data more consistent with the simulated ones, acting as a calibration.

The radios used different crystal oscillators, so the phase measurements were affected by uncertainties. In addition, the phase of the simulated data needed adjustment, as it was difficult to calculate the exact electrical length of the path between the reference planes of Tx and Rx. A further adjustment needed to be made for the amplitudes.

The genetic algorithm (GA) from MATLAB was used for performing this optimization, because of its capability of dealing with non-linear functions with mixed integer/rational parameters and because it is a global search algorithm [32]. As the function being evaluated is not critical in terms of computational cost, other algorithms may also perform well. Note that the cost function uses simulated data from a database generated in the parametric study, that is, a limited set of pre-processed scenarios. Due to this, it was not necessary to run new FEM simulations during the optimization.

The default parameters were used in the GA, except those that are described in the Results section. In total, 10 parameters were to be optimized: the constants $c^{(\text{config})}$ for adjusting the magnitude; the initial index of the samples to be averaged $i^{(\text{config})}$; the distance d to adjust the phase $d^{(\text{config})}$, where the superscript "config" means "AIR", "MUT" or "MET"; and a weight parameter w, which permits using a unique function to optimize both the magnitude and the phase in a multi-objective approach, as explained in detail later.

The vector of the parameters to be optimized was $x_{opt} = [c^{(\text{AIR})}, i^{(\text{AIR})}, d^{(\text{AIR})}, c^{(\text{MUT})}, i^{(\text{MUT})}, d^{(\text{MUT})}, c^{(\text{MET})}, i^{(\text{MET})}, d^{(\text{MET})}, w]$. The defined bounds were: $0.1 \leq c^{(\text{config})} \leq 10$; $750 \leq i^{(\text{config})} \leq 1000$; $1 \leq d^{(\text{config})} \leq 2$ and $0.001 \leq w \leq 0.999$. The bounds for w were not exactly 0 and 1, in order to avoid local solutions that ignored the idea of optimizing both magnitude and phase. The limits for c meant that the scale could be up to 10 times higher or lower. The limits for i in the objective function were multiplied by 2560, discarding the range that was more subject to errors. The limits for d were based on the dimensions of the setup. The wave travels about 0.2 m (in the coaxial cable after the transmitter), plus 2 times $L_{\text{air}} = 0.48$ m (in free space), plus about 0.01 m (MUT thickness), resulting in a total distance of 1.17 m. Considering a multipath reflecting on the floor, the path is about 0.2 m (coaxial cable) plus the distance in free air, which could be approximated by $2\sqrt{(L_{\text{air}}^2 + h^2)}$ plus the thickness of the MUT, where L_{air} is the length of the free space path (antenna to MUT) and h is the height of the antenna above the floor. The result is about 1.54 m.

However, it was expected that the apparent distances would be a few centimeters different due to a few reasons: (a) log-periodic antennas depend on the frequency [11], and the active elements for the frequencies under study are more to the back of the antenna; (b) the dielectric of the coaxial cable slows the wave, which could be interpreted as a longer path at the same velocity [10]; (c) there was an adapter on Rx matching the connectors (antenna and receiver) and the electrical insertion length is usually somewhat greater than the mechanical insertion length [10]; and (d) the relative permittivity of the MUT was greater than 1.

The variables w_0, the probe and the permittivity of the floor were assumed to be fixed in order to not increase computational costs and because the results of the parametric study indicated they were within a reasonable approximation.

2.5.1. The Path Length

An estimate of the effective path can be made by summing the elements of the path weighted by their relative velocities, as in Equation (3) for AIR, Equation (4) for MUT and Equation (5) for MET, where P stands for the perceived path, L_{cable} is the length of the coaxial cable, v_{cable} is the relative velocity in the coaxial cable, L_{air} is the length of the free-space path (antenna to MUT), v_{air} is the relative velocity in free space, L_{mut} is the thickness of the MUT, v_{mut} is the relative velocity in the MUT, L_{adapter} is the length of the adapter in the Rx, v_{adapter} is its relative velocity and h is the height of the antenna above the floor.

$$P^{(\text{AIR})} = \frac{L_{\text{cable}}}{v_{\text{cable}}} + 2\frac{L_{\text{air}}}{v_{\text{air}}} + \frac{L_{\text{mut}}}{v_{\text{air}}} + \frac{L_{\text{adapter}}}{v_{\text{adapter}}}, \tag{3}$$

$$P^{(\text{MUT})} = \frac{L_{\text{cable}}}{v_{\text{cable}}} + 2\frac{L_{\text{air}}}{v_{\text{air}}} + \frac{L_{\text{mut}}}{v_{\text{mut}}} + \frac{L_{\text{adapter}}}{v_{\text{adapter}}}, \tag{4}$$

$$P^{(\text{MET})} = \frac{L_{\text{cable}}}{v_{\text{cable}}} + 2\sqrt{\left(\frac{L_{\text{air}}}{v_{\text{air}}}\right)^2 + \left(\frac{h}{v_{\text{air}}}\right)^2} + \frac{L_{\text{mut}}}{v_{\text{air}}} + \frac{L_{\text{adapter}}}{v_{\text{adapter}}}. \tag{5}$$

The lengths were directly measured by inspection: $h = 0.45$ m, $L_{\text{cable}} = 0.20$ m, $L_{\text{air}} = 0.48$ m, $L_{\text{mut}} = 10.18$ mm and $L_{\text{adapter}} = 30$ mm. $v_{\text{air}} = 1$ is a known constant, and the velocities in the cable and adapter were obtained from datasheets and were found to be $v_{\text{cable}} = 0.7$ and $v_{\text{adapter}} = 0.7$, respectively; v_{mut} is unknown.

Using the above values for the parameters, we obtained approximately $P^{(\text{AIR})} = 1.230$ m and $P^{(\text{MET})} = 1.626$ m, which are about 5% more than the absolute lengths. In turn, $P^{(\text{MUT})}$ depended on v_{mut} and could not be estimated beforehand without knowing the properties of the material, as the velocity depended on it, as shown in Equation (6), where c_0 is the velocity of the wave in vacuum [1]. The result from the optimization permitted this calculation.

$$v = \frac{1}{\sqrt{\mu\varepsilon}} = \frac{c_0}{\sqrt{\mu_r \varepsilon_r}}. \tag{6}$$

Assuming a non-magnetic material under test, that is, $\mu_r = 1$, its real permittivity can be calculated by [1]:

$$\varepsilon_r' = \frac{1}{v_{\text{mut}}^2}. \tag{7}$$

The imaginary part ε_r'' can be approximated by Equation (8), where ΔA is the attenuation in dB and λ_0 is the wavelength in free space [33].

$$\varepsilon_r'' \approx \frac{\Delta A \lambda_0 \sqrt{\varepsilon_r'}}{8.686\pi L_{\text{mut}}}. \tag{8}$$

It is also possible to interpret the problem as a system with the form in Equation (9), where $\mathbf{x}$ are the coefficients to be determined and are related to the relative velocities in the three media, that is, the guided propagation (x_1), the free-space propagation (x_2) and the propagation in the material (x_3).

$$\mathbf{Ax} = \mathbf{b}, \tag{9}$$

where

$$\mathbf{A} = \begin{bmatrix} \left(L_{\text{cable}} + L_{\text{adapt}}\right) & 2L_{\text{air}} + L_{\text{mut}} & 0 \\ \left(L_{\text{cable}} + L_{\text{adapt}}\right) & 2L_{\text{air}} & L_{\text{mut}} \\ \left(L_{\text{cable}} + L_{\text{adapt}}\right) & 2\sqrt{L_{\text{air}}^2 + h^2} + L_{\text{mut}} & 0 \end{bmatrix}, \tag{10}$$

and

$$\mathbf{b} = \begin{bmatrix} d^{(\text{AIR})} & d^{(\text{MUT})} & d^{(\text{MET})} \end{bmatrix}^T. \tag{11}$$

The rows in **A** correspond to the configurations AIR, MUT and MET, respectively, whilst the columns represent the propagation in cables and adapters (first column), air (second column) and tested material (third column).

The calibrated dimensionless velocity v_{mut} is interpreted in Equation (12), in order to normalize it with respect to air, which has the reference velocity, and to subtract the influence of the guided part, which is considered as a phase shift in the optimization, as explained in the following section.

$$v_{\text{mut}} = \frac{1}{\frac{x_3}{x_2} - x_1}. \tag{12}$$

2.5.2. The Error Function

The magnitude error E_m for each configuration is calculated by Equation (13), where x_{opt} is the vector of the parameters to be optimized, S is the simulated data, M is the measured data and $|| \, ||^2$ is the quadratic norm.

$$E_m(x_{opt}) = \frac{||S - M||^2}{||M||^2}. \tag{13}$$

The combined magnitude error from the three configurations is computed by Equation (14).

$$E_m^{(\text{comb})}(x_{opt}) = \frac{1}{3}\left(E_m^{(\text{AIR})} + E_m^{(\text{MUT})} + E_m^{(\text{MET})}\right). \tag{14}$$

The angle ϕ_d of the phase is calculated by Equation (15), where j is the imaginary unit, f is the frequency, v is the velocity of wave and d is the distance in meters. One should note that the optimization runs as if only one v exists in the setup (air)—see the normalization MUT/AIR (x_3/x_2) in Equation (12).

$$\phi_d = \text{angle}\left(e^{-j2\pi\frac{f}{v}d}\right). \tag{15}$$

The adjusted angle ϕ_{Md} of the measured data is given by Equation (16). This shift includes the guided part of the path, which is not modeled in the FEM domain. One should remember that the calibration planes are at the connectors of the radios.

$$\phi_{Md} = \phi_M + \phi_d. \tag{16}$$

The error E_p between the simulated and experimental phase is given similarly to Equations (13) and (14). At last, an overall error E_t can be written in terms of the combined errors and the weighting factor w, as shown in Equation (17).

$$E_t(x) = wE_m^{(\text{comb})} + (1 - w)E_p^{(\text{comb})}. \tag{17}$$

3. Results and Discussion

3.1. Parametric Study

In order to have many possible scenarios, the simulation covered all the possible combinations of the pre-defined values of w_0, complex $\varepsilon_{\text{floor}}$ and probes, for each frequency and for each configuration. This resulted in 286,272 evaluations (3 configurations $\times$ 4 w_0 $\times$ 6 $\varepsilon_{\text{floor (real)}}$ $\times$ 4 $\varepsilon_{\text{floor (imag.)}}$ $\times$ 14 probes $\times$ 71 frequencies). The frequency sweep was configured directly on the FEM software, whilst MATLAB routines updated the values to be simulated.

Several simulated results are in Figure 8. For brevity, only the cases with $w_0 = 0.1$ are shown. Configurations AIR and MUT were quite similar in a broad sense because the MUT had low permittivity and loss. The phase for AIR and MUT were almost linear, whilst in MET, it started around two different values and had different trends along the frequency, depending on the test parameters.

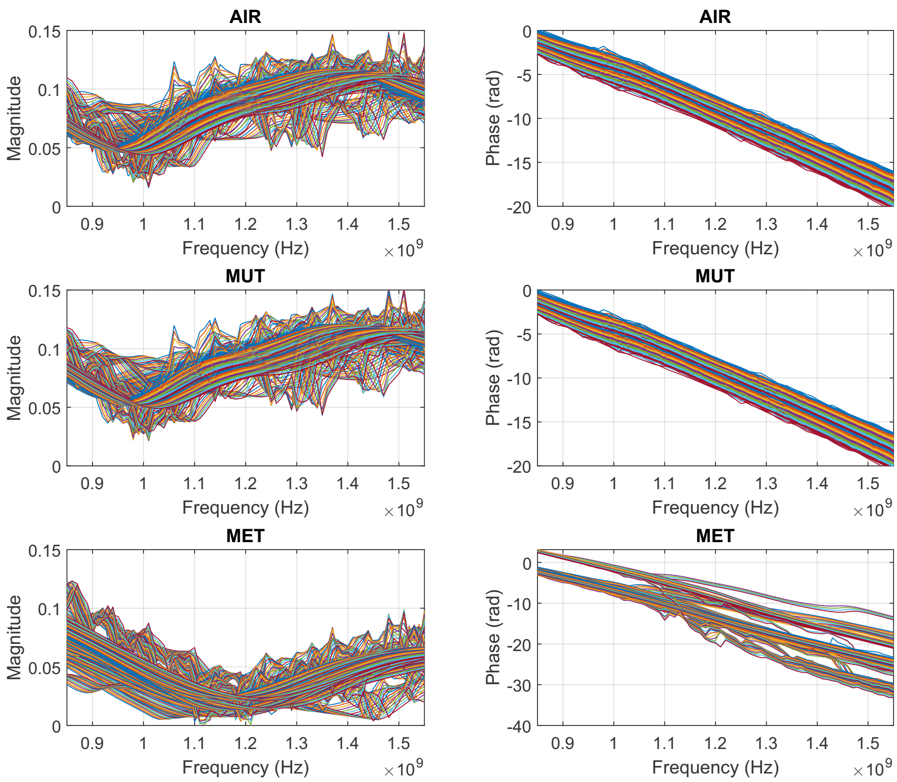

Figure 8. Simulated complex signals for the three configurations, when changing the variable complex ε_r of the floor and the probes in a total of 336 curves. Magnitudes are on the left and phases are on the right. From top to bottom we have AIR, MUT and MET. Due to the number of curves, the phase is unwrapped [1,29] for clarity, and the parameter w_0 is kept constant, equal to 0.1.

3.2. Measured Signals

Regarding the measured signals, Figure 9 shows the mean and standard deviation of the samples from different captures. The first capture presents evident errors, as already explained; thus, it is not shown in Figure 9. For brevity, only the configuration AIR is shown in Figure 9. Despite the efforts in reducing the noises in the experimental setup, some phase noise is still present in the measurements. Much of it, however, is concentrated in specific frequency bands. One can observe that the phase is unstable around the frequencies 0.85, 1.1 and 1.45 GHz. We identified that this can be associated with changes in the RF divider, which is the output divider that divides down the VCO frequency, that is, the oscillator used to synthesize the signal in the transmitter [27]. The ADF4351 VCO operates in the frequency range of 2.2 to 4.4 GHz, as shown in Figure 10, but three dividers have to be used to generate the desired frequencies. More details can be found in [27].

The total error between simulated and measured data is shown in Figure 11, considering the AIR and MUT configurations. We can see how the similarity of the data depends on the virtual probe used to obtain the simulated data and on the complex permittivity of the floor, which are the axes of the subfigures.

Probes closer to the center of the setup (the first probes) tend to sub-estimate the values of the real part and have a more pronounced slope on the level curves. The more distant probes (the last probes) tend to be more centered and have smoother level curves. In general, there were lower errors when the imaginary part was 0.1 and the real part was 5. The fact that these minimum errors were within the bounds chosen for the variables was an indicator that the actual properties were close to the simulated properties.

By the colorbars of Figure 11, one can observe that the lower bound of the scale diminishes as we change the probes (probe 2, probe 4, and so forth). It is consistent with the fact that the positioning of the probes is from the front of the antenna (that is, higher frequencies not used in this work) to behind it (frequencies used).

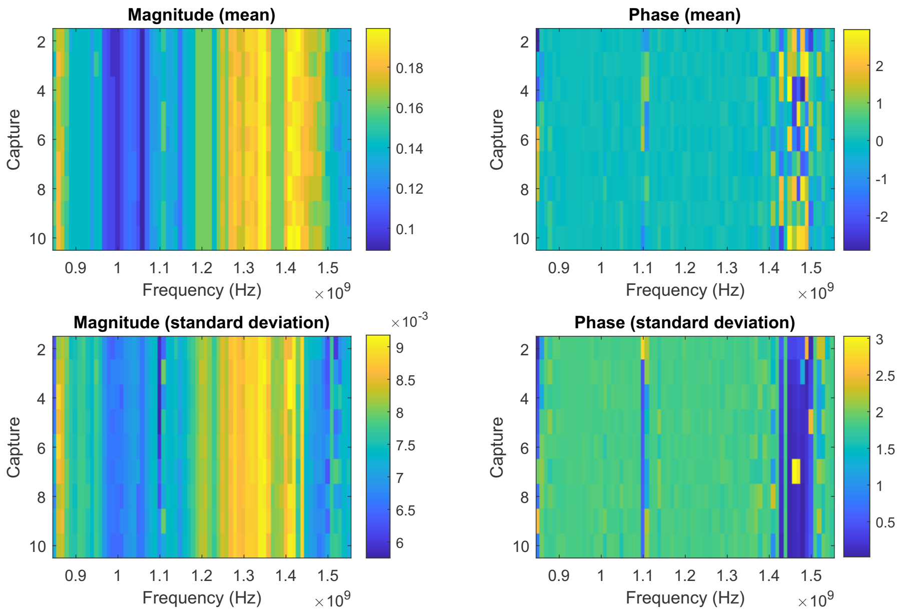

Figure 9. The mean (**top**) and standard deviation (**bottom**) of the frames in the captures of the configuration AIR, both for magnitude (**left**) and phase (**right**). The first capture was omitted because it was always corrupted by errors at the start of the measurement.

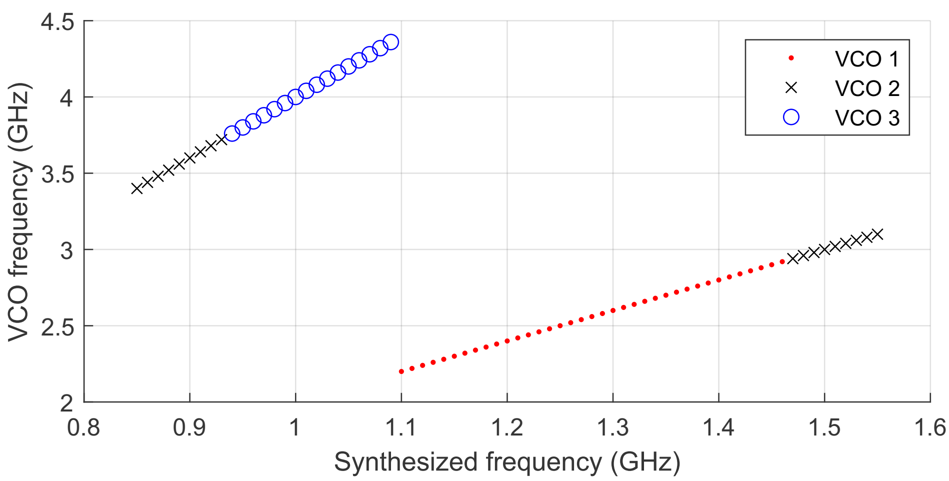

Figure 10. Correspondence between the synthesized frequencies on the transmitter and the three dividers used to generate them, denominated here as VCO 1, VCO 2 and VCO 3.

If the configurations were analyzed separately, AIR and MUT converged to similar values as the probes changed (from the first to the last). This, however, did not happen with the MET, which maintained a real permittivity of about 3 and an imaginary part of 0.1 for all the probes. This is the reason why in Figure 11, the error from MET is not combined with the reported values.

An explanation for this difference is based on how the wave reaches the Rx antenna. The direct path (line of sight) does not exist in the MET configuration and the multi-path is considerably longer than the direct path. The algorithm, however, does not have sufficient information about the propagation, that is, whether it is a situation with a line of sight or a reflected wave, for instance. Therefore, similar values could eventually be obtained from another MUT causing the same delay and attenuation observed in the MET. This lack of differentiation between distinct possibilities makes this inverse problem ill-posed, that is, more than one solution exists for the same fields on the receiver. This corroborates the use of a combined error from the three configurations, as shown in Equation (17).

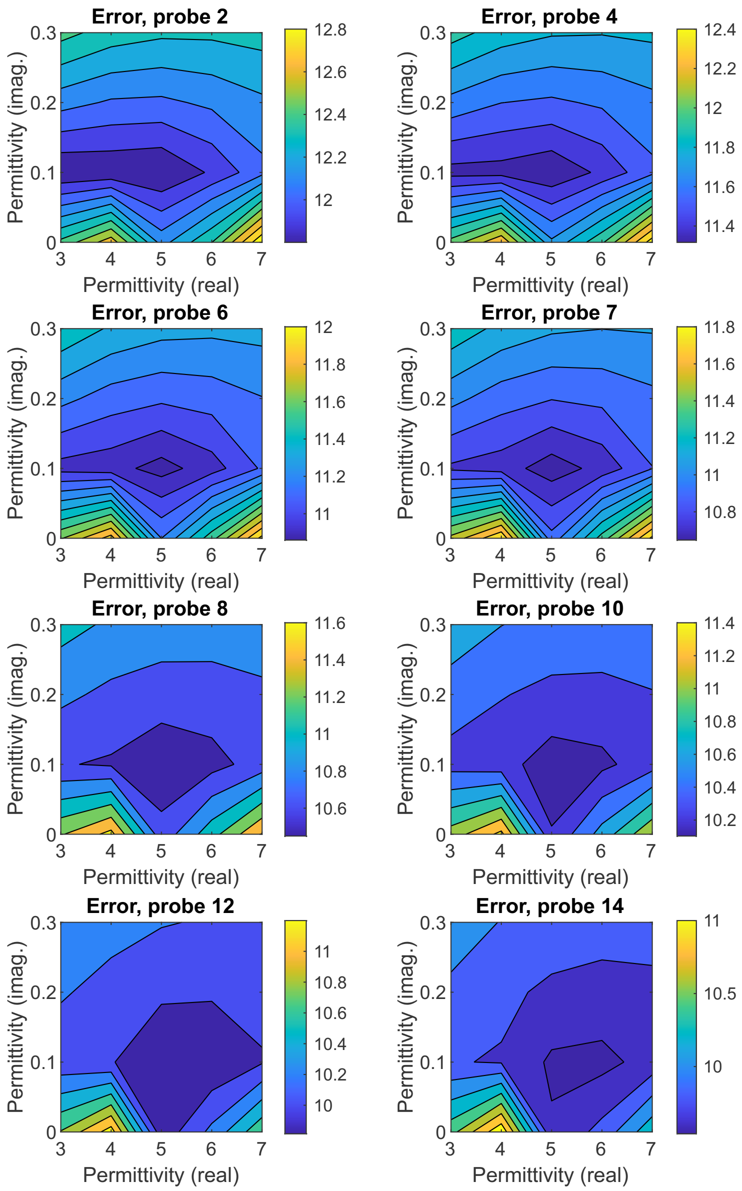

Figure 11. Average error between simulated and measured data, considering AIR and MUT, for different scenarios in which the complex permittivity of the floor and probe were changed. In this case, all the samples were used and the error was not normalized. For brevity, we reported only the even probes (2, 4, 8, 10, 12 and 14) and probe 7, to have an even number of subfigures.

3.3. Optimization

After 1421 iterations, the objective function containing Equation (17) was minimized to 0.57679, with w equal to 0.00100002. The other achieved parameters are shown in Table 1. The value of w was just slightly higher than its lower bound. Although this suggests that it was too bounded, a more wide search range introduces local solutions that affect the convergence. Initially, the GA was not converging to good solutions, then some default options for the stopping criteria were changed to obtain more evaluations: (a) the number of generations was set to be 100 times more than the default, which was 100 times the number of variables; (b) the stall generations, which is 50 at default, was changed to 500; and (c) the function tolerance, which is 10^{-6} by default, was changed to 10^{-9}.

Table 1. Optimized parameters for the three configurations.

	AIR	MUT	MET
c	1.9213	1.9500	1.2155
i	956	917	849
d	1.1932	1.2025	1.6187

The measured signals and the signals simulated by using the optimized values are compared in Figure 12. In the simulation, we used $\varepsilon_{r(\mathrm{MUT})} = 2.61$, $\varepsilon_{r(\mathrm{floor})} = 5.31$ and $\sigma_{(\mathrm{floor})} = 0.02$ S/m [31]. For simplicity, dispersion was not considered. We note a few interesting observations from the results.

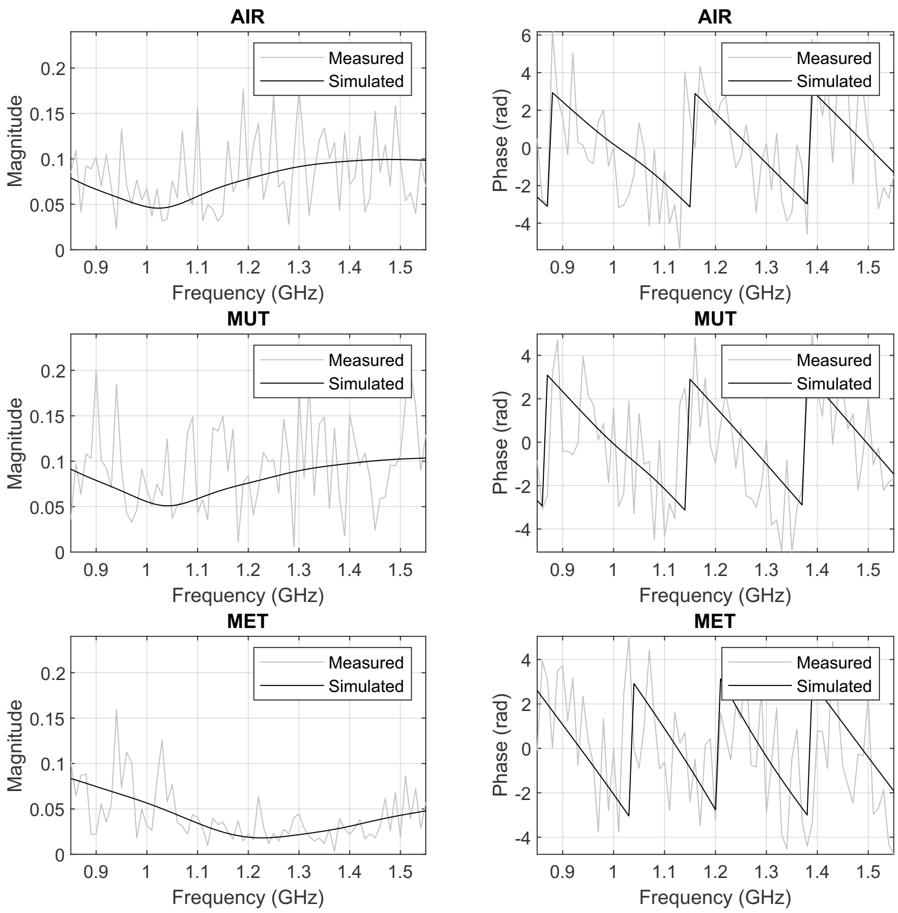

Figure 12. Measured and simulated complex signals for the three configurations, using the optimized values of Table 1. Magnitudes are on the left and phases are on the right. The configurations from top to bottom are AIR, MUT and MET.

From Table 1, we see that the constant $c^{(\mathrm{MET})}$ is quite different from $c^{(\mathrm{AIR})}$ and $c^{(\mathrm{MUT})}$. It is consistent with the fact that less energy reaches the receiver when the line of sight is blocked by the metal, particularly in the higher frequencies, as seen in Figure 12.

We suggest that the c values for AIR and MUT were quite similar as the MUT is a low-loss material and does not cause much attenuation to the signal. One can see in Figure 12 that the magnitude of the MUT has more variability, with a few values discrepant from the reference, for instance, two in the region of 0.9–0.95 GHz and others just above 1.5 GHz.

The indexes i of the samples were consistent with the empiric observations that the last samples were less subjected to errors. The $i^{(\mathrm{AIR})}$ and $i^{(\mathrm{MUT})}$ were closer to the upper bound than to the lower bound, whilst the $i^{(\mathrm{MET})}$ was a little lower, but still had a high value.

The d values for adjusting the phases were compatible with the electrical path traveled by the wave. This path was slightly longer than the physical path, as the wave propagated slowly in the coaxial cable and connectors. The antennae could also introduce some variation in phase, which was not considered here. A further observation was that $d^{(\mathrm{MUT})}$ was about 0.01 m longer than $d^{(\mathrm{AIR})}$, which was consistent with the nominal thickness of the sample (1 cm) that occupied the center of the setup in the MUT configuration.

The $d^{(\mathrm{MET})}$ was a little higher than the estimated multi-path, suggesting that most of the power took a less direct path. Due to the frequency-dependent directivity, we expect that the power received at the lower frequencies is higher than that received at the higher frequencies.

It is worth remembering that a 2D model can limit the accuracy of an analysis. This may be more significant in the MET configuration, as the line of sight was blocked and the three dimensional nature of the reflected and diffracted electromagnetic fields was more difficult to approximate with a simpler model.

We can observe in Figure 12 that the initial phase (at 0.85 GHz) of the MET was in agreement with part of the results presented in Figure 8, that is, a positive value, in contrast to values from AIR and MUT, which always had negative initial values.

Figure 13 shows the simulated z component of the electric field (perpendicular to the plane) for the configuration MET at the last frequency on the range, that is, 1.55 GHz. It is possible to note that the region of the receiving antenna was subjected to fields partially reflected on the floor, in accordance with the estimated and discussed behavior of the wave.

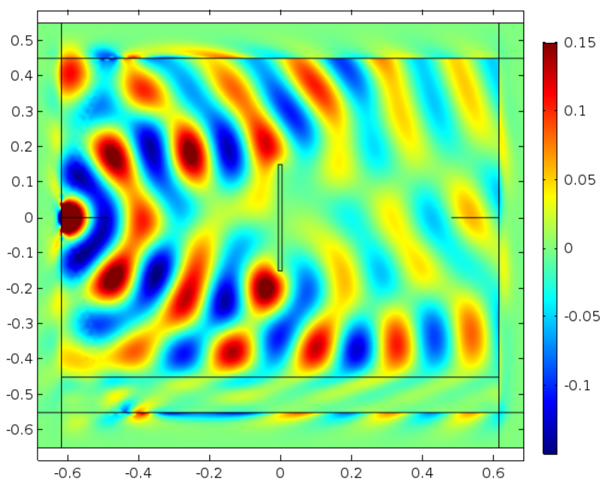

Figure 13. The simulated z component of the electric field (E_z) at 1.55 GHz, when the configuration is MET. One can observe the difference between the superior and inferior halves of the open-space domain, due to the reflection on the floor. In this simulation, $-0.37 \leq E_z \leq 0.40$ V/m. For better contrast, the color range was set to ± 0.15. The in-plane coordinates x (horizontal) and y (vertical) are in meters.

Using the values d in Table 1 to form $\mathbf{b}$ in Equation (11), solving Equation (9), we get $\mathbf{x} = [0.1447; 1.1956; 2.1084]$, $v_{\text{mut}} = 0.6178$ and $\varepsilon_r' = 2.6204$. Regarding the imaginary part, as shown in Equation (8), assuming $\Delta A = c^{(\text{MUT})} - c^{(\text{AIR})}$, at the intermediate frequency 1 GHz ($\lambda_0 = 0.3$ m), one obtains $\varepsilon_r'' = 0.05$. This value is the same reported in [24], but it is higher than the reference [23], although it is still within the uncertainty levels reported there. Actually, the computational model used here assumed a lossless MUT and a nondispersive floor, which could contribute to this difference.

4. Conclusions

This work dealt with affordable SDRs without clock synchronization, in an attempt to explore their possible ability to perform free-space measurements, to be used in the estimation of electromagnetic permittivity .

Despite the intrinsic limitations of the hardware, due to the low cost of the prototype setup, we believe that the study has led to some interesting results for the permittivity estimation. The proposed technique relies on the numerical simulation of the measurement configuration, which is used as a sort of calibration stage, leaving to the comparison with the actual measured data the task of recovering the values of the DUT parameters. So, the technique could be used in different environments and configurations just by changing some of the computational parameters. Several expedients have been explored to address the limitations of the setup and, in the perspective of a cost-benefit compromise, the experimental data turned out to be consistent with simulations and with other references.

This indicates that a sufficient amount of data exploited in conjunction with a computational model can, under certain circumstances, compensate for the absence of synchrony between Tx and Rx and overcome other drawbacks of a low-cost setup.

The paper provides a preliminary study focused on many aspects of the characterization problem (setup, software, hardware, model, electromagnetics). Each of these aspects deserves a deeper investigation in future works including: (a) the free-space calibration; (b) optimization of parameters like the permittivity of the MUT, the properties of the floor and w_0; (c) improving the computational model, possibly in 3D; (d) developing the uncertainty analysis.

Author Contributions: Conceptualization, F.J.F.G. and E.J.D.S.; Methodology, F.J.F.G. and E.J.D.S.; Software, F.J.F.G. and L.A.F.; Validation, F.J.F.G., A.B. and E.J.D.S.; Formal analysis, F.J.F.G., A.B. and E.J.D.S.; Investigation, F.J.F.G. and L.A.F.; Resources, F.J.F.G. and L.A.F.; Data curation, F.J.F.G.; Writing—original draft, F.J.F.G.; Writing—review & editing, F.J.F.G., A.B., L.A.F. and E.J.D.S.; Supervision, E.J.D.S.; Project administration, F.J.F.G. and AB. All authors have read and agreed to the published version of the manuscript.

Funding: This research was funded by: Ministero dello Sviluppo Economico, within the program UE-FESR, PON "Imprese e competitività" 2014–2020, under the project "IDROS" (Impiego di Droni per la Ricerca nel sottOSuolo) grant number F/050187/02/X32; Conselho Nacional de Desenvolvimento Científico e Tecnológico (CNPq) and Fundação de Amparo à Pesquisa do Estado de Minas Gerais (FAPEMIG) under grant number APQ-03382-17.

Institutional Review Board Statement: Not applicable.

Informed Consent Statement: Not applicable.

Data Availability Statement: The data presented in this study are available on request from the corresponding author.

Conflicts of Interest: The authors declare no conflict of interest.

References

1. Chen, L.; Ong, C.; Neo, C.; Varadan, V.; Varadan, V. *Microwave Electronics—Measurement and Materials Characterization*; John Wiley & Sons, Inc.: Hoboken, NJ, USA, 2004.
2. Collier, R.; Skinner, D. (Eds.) *Microwave Measurements*, 3rd ed.; IET: London, UK, 2007.
3. Liu, X.; Gan, L.; Yang, B. Millimeter-wave free-space dielectric characterization. *Measurement* **2021**, *179*, 109472. [CrossRef]

4. Hasar, U.C.; Kaya, Y.; Ozturk, G.; Ertugrul, M.; Korasli, C. Broadband, Stable, and Noniterative Dielectric Constant Measurement of Low-Loss Dielectric Slabs Using a Frequency-Domain Free-Space Method. *IEEE Trans. Antennas Propag.* **2022**, *70*, 12435–12439. [CrossRef]
5. Aman, Vineet Singh, N.S.B. A free space frequency-time-domain technique for electromagnetic characterization of materials using reflection-based measurement. *Int. J. Microw.-Comput.-Aided Eng.* **2021**, *31*, 1–12. [CrossRef]
6. Sagnard, F.; El Zein, G. Characterization of building materials for propagation modelling: Frequency and time responses. *AEU—Int. J. Electron. Commun.* **2005**, *59*, 337–347. [CrossRef]
7. Davis, B.; Grosvenor, C.; Johnk, R.; Novotny, D.; Baker-Jarvis, J.; Janezic, M. Complex Permittivity of Planar Building Materials Measured With an Ultra-Wideband Free-Field Antenna Measurement System. *J. Res. Natl. Inst. Stand. Technol.* **2007**, *112*, 67. [CrossRef]
8. Pisa, S.; Pittella, E.; Piuzzi, E.; D'Atanasio, P.; Zambotti, A. Permittivity measurement on construction materials through free space method. In Proceedings of the 2017 IEEE International Instrumentation and Measurement Technology Conference (I2MTC), Torino, Italy, 22–25 May 2017; pp. 1–4. [CrossRef]
9. Brancaccio, A.; D'Alterio, G.; De Stefano, E.; Di Guida, L.; Feo, M.; Luce, S. A free-space method for microwave characterization of materials in aerospace application. In Proceedings of the 2014 IEEE Metrology for Aerospace (MetroAeroSpace), Benevento, Italy, 29–30 May 2014; pp. 423–427. [CrossRef]
10. Hiebel, M. *Fundamentals of Vector Network Analysis*, 5th ed.; Rohde & Schwarz: München, Germany, 2011.
11. Balanis, C.A. *Anntena Theory—Analysis and Design*, 2nd ed.; John Wiley & Sons: Hoboken, NJ, USA, 1997.
12. Collins, T.F.; Getx, R.; Pu, D.; Wyglinski, A.M. *Software-Defined Radio for Engineers*, 1st ed.; Artech House: Norwood, MA, USA, 2018.
13. Akcelik, H.; Durna, Y.; Saraydemir, S.; Kocer, H. Measurement of a metamaterial antenna angular power reception performance utilizing Software Defined Radio. *AEU—Int. J. Electron. Commun.* **2017**, *75*, 91–97. [CrossRef]
14. Debatty, T. Software defined RADAR a state of the art. In Proceedings of the 2010 2nd International Workshop on Cognitive Information Processing, Elba Island, Italy, 14–16 June 2010; pp. 253–257. [CrossRef]
15. Costanzo, S.; Spadafora, F.; Massa, G.D.; Borgia, A.; Costanzo, A.; Aloi, G.; Pace, P.; Loscri, V.; Moreno, H.O. Potentialities of USRP-Based Software Defined Radar Systems. *Prog. Electromagn. Res. B* **2013**, *53*, 417–435. [CrossRef]
16. Costanzo, S.; Spadafora, F.; Moreno, O.H.; Scarcella, F.; Massa, G.D. Multiband Software Defined Radar for Soil Discontinuities Detection. *J. Electr. Comput. Eng.* **2013**, *2013*, 1–6. [CrossRef]
17. Cerquera, M.R.P.; Montaño, J.D.C.; Mondragón, I. UAV for Landmine Detection Using SDR-Based GPR Technology. In *Robots Operating in Hazardous Environments*; Canbolat, H., Ed.; IntechOpen: Rijeka, Croatia, 2017; Chapter 2; pp. 25–58. [CrossRef]
18. Chuma, E.L.; Iano, Y.; Roger, L.L.B.; Fontgalland, G. Measuring dielectric properties by two methods using software-defined radio. *IET Sci. Meas. Technol.* **2019**, *13*, 1003–1008 . [CrossRef]
19. Aloi, G.; Loscrí, V.; Borgia, A.; Natalizio, E.; Costanzo, S.; Pace, P.; Di Massa, G.; Spadafora, F. Software Defined Radar: Synchronization Issues and Practical Implementation. In Proceedings of the 4th International Conference on Cognitive Radio and Advanced Spectrum Management, Barcelona Spain, 26–29 October 2011; CogART '11; Association for Computing Machinery: New York, NY, USA, 2011; pp. 1–5. [CrossRef]
20. Bourreau, D.; Péden, A. Solid and Non-Solid Dielectric Material Characterization for Millimeter and Sub-Millimeter Wave Applications. In Proceedings of the 2020 50th European Microwave Conference (EuMC), Utrecht, The Netherlands, 12–14 January 2021; pp. 909–912. [CrossRef]
21. Chung, J.Y. Broadband Characterization Techniques for RF Materials and Engineered Composites. Ph.D. Thesis, The Ohio State University, Columbus, OH, USA, 2010.
22. Davidson, D.B. *Computational Electromagnetics for RF and Microwave Engineering*, 2nd ed.; Cambridge University Press: Cambridge, UK, 2011.
23. Gonçalves, F.J.F.; Pinto, A.G.; Mesquita, R.C.; Silva, E.J.; Brancaccio, A. Free-Space Materials Characterization by Reflection and Transmission Measurements using Frequency-by-Frequency and Multi-Frequency Algorithms. *Electronics* **2018**, *7*, 260. [CrossRef]
24. Baker-Jarvis, J.; Janezic, M.; Riddle, B.; Johnk, R.; Holloway, C.; Geyer, R.; Grosvenor, C. Measuring the Permittivity and Permeability of Lossy Materials: Solids, Liquids, Metals, and negative-Index Materials. Technical Note (NIST TN) 1536, National Institute of Standards and Technology, Gaithersburg, MD, USA, 2005. Available online: https://nvlpubs.nist.gov/nistpubs/Legacy/TN/nbstechnicalnote1536.pdf (accessed on 21 February 2023).
25. Stewart, R.W.; Barlee, K.W.; Atkinson, D.S.W.; Crockett, L.H. *Software Defined Radio Using MATLAB & Simulink and the RTL-SDR*, 1st ed.; Strathclyde Academic Media: Glasgow, Scotland, UK, 2015.
26. GNU Radio Project. 2022. Available online: https://www.gnuradio.org (accessed on 10 March 2022).
27. Analog Devices. *ADF4351 Wideband Synthesizer with Integrated VCO*; Data Sheet, Rev. A.; Analog Devices: Norwood, MA, USA, 2017.
28. Holdsworth, J. Pyadf43x, A Package for Automating AD4350/1 Boards. 2018. Available online: http://github.com/jhol/pyadf435x (accessed on 9 March 2022).
29. Hopcraft, K.; Smith, P.R. *An Introduction to Electromagnetic Inverse Scattering*, 1st ed.; Kluwer Academic Publishers: Dordrecht, The Netherlands, 1992.

30. Büyüköztürk, O.; Yu, T.Y.; Ortega, J.A. A methodology for determining complex permittivity of construction materials based on transmission-only coherent, wide-bandwidth free-space measurements. *Cem. Concr. Compos.* **2006**, *28*, 349–359. [CrossRef]
31. ITU. *Effects of Building Materials and Structures on Radiowave Propagation Above About 100 MHz*; Recommendation ITU-R P.2040-1; P Series Radiowave Propagation, Electronic Publication; International Telecommunication Union Radiocommunication Sector: Geneva, Switzerland, 2021.
32. Mathworks. MATLAB Genetic Algorithm: Genetic Algorithm Solver for Mixed-Integer or Continuous-Variable Optimization, Constrained or Unconstrained. 2019. Available online: https://www.mathworks.com/help/gads/genetic-algorithm.html (accessed on 26 May 2022).
33. Trabelsi, S.; Kraszewski, A.; Nelson, S. Phase-shift ambiguity in microwave dielectric properties measurements. *IEEE Trans. Instrum. Meas.* **2000**, *49*, 56–60. [CrossRef]